Injection of intense low-energy reactor-based positron beams into a supported magnetic dipole trap

Plasma Research Express

PAPER

Injection of intense low-energy reactor-based positron beams into a supported magnetic dipole trap

J Horn-Stanja[1], E V Stenson[1,2,3], M R Stoneking[1,4], M Singer[2,1], U Hergenhahn[1,5], S Nißl[1,2], H Saitoh[1,6], T Sunn Pedersen[1,7], M Dickmann[2], C Hugenschmidt[2] and J R Danielson[3]

[1] Max Planck Institute for Plasma Physics, 85748 Garching and 17491 Greifswald, Germany
[2] Technische Universität München, 85748 Garching, Germany
[3] University of California San Diego, La Jolla, California 92093, United States of America
[4] Lawrence University, Appleton, Wisconsin 54911, United States of America
[5] Fritz-Haber-Institut der Max-Planck-Gesellschaft, 14195 Berlin, Germany
[6] The University of Tokyo, 277-8561 Kashiwa, Japan
[7] University of Greifswald, 17489 Greifswald, Germany

E-mail: juliane.stanja@ipp.mpg.de

Keywords: electron-positron plasma, positron beam, dipole magnetic field

OPEN ACCESS

RECEIVED
30 October 2019

REVISED
10 January 2020

ACCEPTED FOR PUBLICATION
23 January 2020

PUBLISHED
30 January 2020

Abstract

An increased low-energy positron flux is obtained from the reactor based NEPOMUC source when using its primary beam at energies as low as 20 eV. First experiments with this beam in a supported magnetic dipole trap resulted in the maximum current of injected positrons to date. According to single-particle simulations, remaining limitations in the injection efficiency, observed in the experiment, can be attributed to the spatial spread of the beam. In the first trapping measurements with this beam, top-down asymmetries in the electrostatic trapping potential are found to be detrimental to confinement.

1. Introduction

The APEX (A Positron Electron eXperiment) project aims for the first creation of a magnetically confined electron-positron pair plasma in the laboratory [1]. One promising candidate for the confining magnetic field structure is that of a magnetic dipole since it offers, amongst others, neutral and non-neutral plasma confinement, as seen in planetary magnetospheres and the laboratory [2–5]. Currently, a supported permanent magnet trap is being used at the open beam port of the Neutron-induced positron source Munich (NEPOMUC) [6, 7] to establish key techniques, such as injection [8, 9]. Meanwhile, design studies for a levitated dipole trap, which will contain the two species at plasma densities, are ongoing [10].

Although the creation of the pair plasma from dissociation of positronium has been proposed [1], the experimental implementation of this method has not been addressed to date. Instead, direct injection of electron and positron beams using an $E \times B$ drift scheme is being pursued for introducing charged particles into the trap. Following the first promising results [8], eventually lossless injection was achieved [9] with the low-energy, high-brightness remoderated positron beam from NEPOMUC. The total number of injected and trapped positrons is small, however, due to the combination of short ($\sim 10\mu$s) transit times through the trap and the available flux of remoderated positrons ($1–3 \cdot 10^7$ e^+/s). To increase this would require a stronger source or, for example, stacking of multiple bunches into the trap. Although the latter has been successfully demonstrated for linear traps [11, 12], its implementation for a magnetic dipole trap using a reactor-based source is not straightforward.

Here, we focus on the former using an obvious candidate for a stronger source: the lower-brightness but higher-flux NEPOMUC primary beam which is usually extracted with an energy of one thousand electron-volts (eV). As the target energy for the pair plasma components is only a few eV, a beam of accordingly low kinetic energy had to be prepared and characterized first. Subsequently, its suitability for injection and trapping in the supported magnetic dipole trap had to be verified.

In the following, we review the setup of the positron source as well as the apparatus for beam characterization and dipole experiments. After discussing the low-energy primary beam characteristics, the

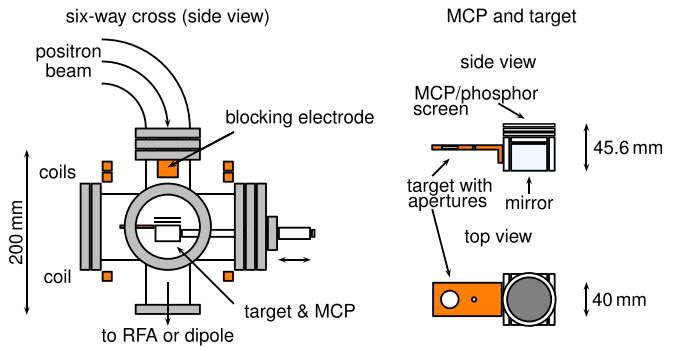

Figure 1. (Left) Schematic side view of the six-way cross with beam control and diagnostics installed immediately upstream of the main experimental chamber (RFA: retarding field analyzer). (Right) Schematic side and top views of the microchannel plate (MCP) and target.

results from dipole injection experiments along with complementary simulations are presented. Finally, results from first trapping experiments with the low-energy primary beam are shown.

2. Experimental setup

2.1. NEPOMUC primary beam

The reactor-based positron source NEPOMUC [6] is operated at the research neutron source Heinz Maier-Leibnitz (FRM II) of the Technical University Munich. At NEPOMUC, thermal neutrons are captured in a ^{113}Cd-enriched cap inside the tip of an experimental beam tube, which results in the emission of energetic γ-rays from ^{114}Cd. In an adjacent structure of platinum foils, positrons are generated by pair production and moderated. The platinum foils are typically set to an electrostatic potential of 1kV in order to extract and accelerate the moderated positrons to a beam energy of 1 keV. The beam with a maximum flux of $1 \cdot 10^9\, e^+/\mathrm{s}$ [7] is transported by means of a magnetic guiding field of ~5 mT, resulting in a typical beam diameter of about 10 mm (FWHM). For most experiments this primary positron beam is brightness-enhanced using a tungsten single crystal in reflection geometry inside a remoderation device further downstream. In this work, however, we make use of the primary positron beam itself and tailor its energy to the requirements of our experiments.

2.2. Beam diagnostics

The primary positron beam was guided magnetically to our experiment. A six-way cross with a magnetic field coil set provides the permanent part of the beam diagnostics (figure 1). A cylindrical blocking electrode (deflector) is located at the beam's entrance. A target with two apertures (3- and 15-mm diameter) and a microchannel plate (MCP; with a phosphor screen, 25-mm diameter) can be inserted on the midplane of the cross using a linear feedthrough.

A rough measurement of the parallel energy results from scanning the bias of the blocking electrode while observing either the annihilation signal, seen by a scintillation detector looking at the target, or the image from the MCP's phosphor screen, reflected by a 45° mirror and captured with a CCD camera. The total positron flux entering the experiment is determined by inserting the target into the beam line and connecting it to a current-integrating amplifier. The image of the beam from the MCP's phosphor screen yields information about its shape, size and centering. The centering can be confirmed by inserting the apertures, while monitoring the annihilation signal or the current.

To further diagnose the energy distribution of the beam, a retarding field analyzer (RFA) can be temporarily installed downstream of the six-way cross, as described in a previous publication [13]. It consists of a 15-mm aperture, a cylindrical retarding electrode and a collector in an adjustable magnetic field region. The view of a bismuth germanate (BGO) scintillation detector ($d = 22\mathrm{mm}, l = 25$ mm, from Korth Kristalle, with Hamamatsu type H10425 photomultiplier) is collimated to detect annihilation gamma rays from the collector plane. Measurements of the parallel energy distribution in various final magnetic fields provide information about the mean perpendicular energy [14].

2.3. The supported magnetic dipole trap

Alternately, a supported magnetic dipole trap can be installed downstream from the six-way cross described in the previous section. This setup has been used in [8, 9] and is described here for completeness. The axes of the beam line magnetic field and the magnet are parallel but not aligned. Two pairs of steering coils immediately

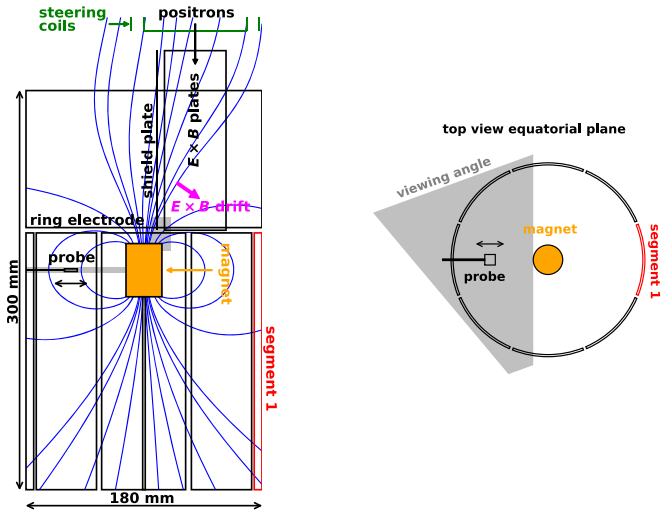

Figure 2. (Left) Schematic side view of the electrodes installed inside the dipole trap. In addition, the lower parts of the steering coils at the entrance to the dipole trap are indicated by green lines, and the outer wall segment 1 is drawn in red. The magnetic field lines are shown in blue. The gray boxes indicate the collimation of two BGO scintillation detectors used in this study. (Right) Cross section through the equatorial plane showing the viewing angle of the BGO scintillation detector that is aimed at the movable probe.

upstream from the trap's entrance can be used to fine-tune the beam position. The trap itself consists of a supported cylindrical neodymium magnet (field strength of 0.6T at its poles) in a tight copper case, surrounded by a segmented cylindrical outer wall (1 ring electrode at the top and 8 segments at the bottom), as shown in figure 2. Together with the magnetic field, a perpendicular electric field generated by a pair of oppositely biased electrodes ($E \times B$ plates) at the trap's entrance induces an $E \times B$ drift that transports charged particles across magnetic field lines. This drift is employed in order to guide the beam from the (off-axis) beam line magnetic field into the confinement region. The details of the injection process are described in [9]. To diagnose the positrons that have been successfully injected and their radial distribution in the trap after a half toroidal transit (due to toroidal grad-B and curvature drifts), a radially insertable probe is installed in the equatorial plane of the trap, opposite the injection region. The probe is viewed by a collimated BGO scintillation detector (with the same technical specifications as described in the previous section) and can, in addition, be connected to a current-integrating amplifier.

3. Beam characteristics at the experiment

At NEPOMUC, the primary positron beam has been extracted from the source section with kinetic energies comparable to those used in previous experiments with the remoderated beam, i.e. 5 and 20 eV, for the first time. For this purpose, the extraction potentials of the electrostatic lenses and the magnetic guiding fields had to be adjusted, taking into account several experimental constraints such as availability of bipolar high-power supplies and limited beam time. Particularly at low kinetic energy, transport losses due to imperfect beam guiding of the primary beam between the source and the experiment are expected to reduce the beam intensity. In the following, we give the characteristics of the low-energy primary beams as transported to the entrance of the magnetic dipole trap.

3.1. 5-eV beam

For the lowest-energy primary beam, with about 5 eV of parallel energy, an average intensity of $(2.3 \pm 0.9) \cdot 10^7\ e^+/\mathrm{s}$ was measured at our experiment. This beam was accompanied by a significant electron component. In previous studies at the first accessible point of the positron beam facility (close to the biological shield of the reactor), pair production, Compton- and photo-effect inside the beam tube have been identified as the origin of these electrons (up to energies of a few 100 eV). In principle, by finding different positron beam settings, these electrons can be efficiently suppressed [15].

To quantify the corresponding fluxes of electrons and positrons, the beam flux to the target in the six-way cross was measured with a current-integrating amplifier for different bias voltages of the blocking electrode (figure 3). When the blocking electrode is grounded or has a slightly negative bias, the signal is dominated by the electron flux. It is about 60 times the positron flux, which can be observed with biases below −100 V. The measured positron flux is the same order of magnitude as the 5-eV remoderated beam (table 1). Furthermore, the measurement reveals that the electron energy distribution is very broad, extending up to 100 eV. The signal

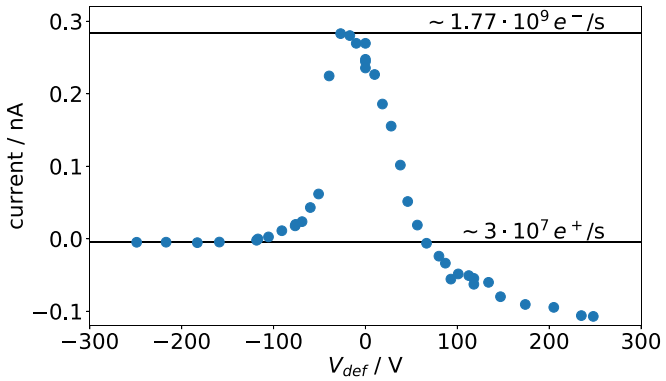

Figure 3. Current measured at the target in the six-way cross upstream from the dipole trap's entrance for various bias voltages to the blocking electrode. The horizontal lines mark the corresponding maximum electron flux (reduced by the saturated positron flux) and the saturated positron flux, respectively.

Table 1. Mean beam flux measured in the six-way cross at the experiment's entrance for the remoderated (r) and primary (p) beam energies discussed in this paper.

Beam energy [eV]	Type	Flux [10^7 e^+/s]
5	r	1.8 ± 0.5
5	p	2.3 ± 0.9
22	r	5 ± 2
20	p	13 ± 1

Table 2. Minimum and maximum spatial beam extents (FWHM) for the remoderated (r) and primary (p) beam energies discussed in this paper. The extents have been determined by the method described in the text. One specific example is illustrated in figure 5 for the 20-eV primary beam.

Beam energy [eV]	Type	$FWHM_{min}$ [mm]	$FWHM_{max}$ [mm]
5	r	2.3 ± 0.1	3.8 ± 0.4
5	p	6.3 ± 0.7	12 ± 3
22	r	2.6 ± 0.1	4 ± 1
20	p	7.7 ± 0.4	13 ± 2

shape for positive biases of the blocking electrode is attributed to secondary electrons produced by the incoming electron beam which, depending on the surface condition of the target and the primary electron energy, can exceed the primary electron flux [16]. These secondaries are then able to leave the target, effectively reducing the measurable flux.

The spatial extent of the positron beam is determined from the background-subtracted MCP images. As the beam spot is not necessarily aligned with the image grid it was rotated in steps of 5°. For each orientation, the maximum of the sum of all columns and of all rows, respectively, was identified. From the locations of the points at half the maximum intensity the beam spread was calculated. As characteristic quantity for the spatial extent of the positron beam we quote its minimal and maximal size (FWHM) from all orientations. We note that, at least for the primary beam, its shape generally deviates from a 2D Gaussian. At 5 eV, the width of the primary beam was determined to be 6–12 mm, compared to 2–4 mm for the remoderated beam (table 2).

The RFA setup was used to measure the energy of the centered 5-eV primary beam without an aperture, with the 3-mm aperture, and with the 15-mm aperture inserted. During all measurements, the collector bias voltage was set to −20 V, and the annihilation gamma rays from the collector plate were measured as a function of the retarding electrode bias. For each aperture, at least one data set was taken in a homogeneous magnetic field of 4.8 mT, and in field gradients with five different final magnetic fields B_f. Data sets from identical conditions have been averaged. The averaged data has been smoothed and its derivative is used to determine the mean parallel

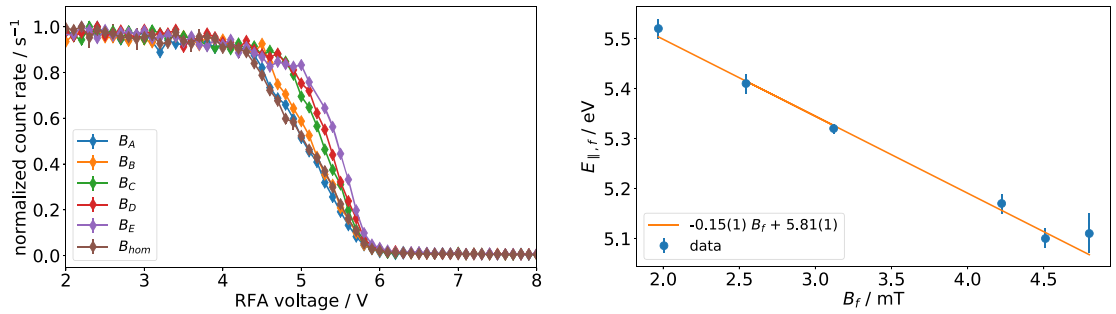

Figure 4. (Left) RFA measurements for the 5-eV primary beam with a 15-mm aperture inserted upstream, for various magnetic field gradients with final magnetic fields $B_{hom} > B_A > B_B > B_C > B_D > B_E$. (Right) Resulting variation of the mean parallel energy as a function of final magnetic field and the corresponding maximum likelihood fit.

Table 3. Energy measurements of the 5-eV primary beam (p) in a final magnetic field of 4.8 mT for three different aperture settings. For comparison, the results for the 5-eV remoderated beam (r) from [13] are quoted for the same field.

Type	Aperture	$\bar{E}_{tot}$ [eV]	$\bar{E}_{\perp}/B_i$ [eV/mT]	$E_{\parallel}$ [eV]	$\sigma_{E_{\parallel}}$ [eV]
p	none	5.76(1)	0.14(1)	5.09(5)	0.628(4)
p	3 mm	5.72(1)	0.12(1)	5.14(5)	0.586(4)
p	15 mm	5.81(1)	0.15(1)	5.09(5)	0.68(1)
r	5 mm	5.94(2)	0.16(1)	5.18(2)	0.78(2)

energy and the energy spread. Assuming a linear relation, the maximum likelihood method yields a slope m and intercept n from the variation of the mean parallel energy with the final magnetic field. The slope equals $m = -\bar{E}_{\perp}/B_i$ and the intercept is $n = \bar{E}_{tot}$, where $\bar{E}_{\perp}$ is the initial mean perpendicular energy, $\bar{E}_{tot}$ is the mean total beam energy, and B_i is the birth magnetic field. Examples of the RFA measurements and the resulting variation of the mean parallel energy with magnetic field are shown in figure 4. The numerical results for all three conditions are given in table 3.

A comparison of the energy characteristics of the 5-eV primary and remoderated beam (table 3) with no magnetic field gradient ($B_f = 4.8$ mT) yields a slightly lower mean total, parallel and perpendicular energy (over B_i) as well as parallel spread for the primary beam.

3.2. 20-eV beam

From the point of view of our larger project goals, the intensity of a 5-eV primary beam in the present measurement is not a substantial improvement over the remoderated beam at the same energy. Moreover, its larger spatial spread measured at our experiment is undesirable from the viewpoint of injection into the dipole trap, as discussed below. A modest increase in the primary beam energy to 20 eV, however, offered improved characteristics. For the primary beam at 20 eV, an electron component of approximately the same magnitude as the positron flux was observed in the beam tube close to the biological shield of the reactor, but this could not be detected at our experiment. There, a mean positron flux of $1.3(1) \cdot 10^8$ e$^+$/s was measured on the target in the six-way cross, which is a factor of 2.6 higher than the mean flux of the remoderated beam at comparable energy (22 eV), as given in table 1.

The spatial extent of the 20-eV positron beam was determined as described in the previous section. It is 8–13 mm for the primary beam, as compared to 3–4 mm for the 22-eV remoderated beam (table 2). Examples of MCP images for both beams are shown in figure 5.

With the RFA setup, the 20-eV primary beam energy was measured before and after centering the beam without an upstream aperture in the homogeneous magnetic field and with five magnetic field gradients. With the 3-mm aperture inserted upstream, data was taken in the homogeneous field and with three field gradients. The collector bias voltage was again set to −20 V. The same data analysis as for the 5-eV primary beam was performed. The numerical results for the three conditions are given in table 4.

The parallel spread and mean perpendicular energy (over B_i) of the 20-eV primary beam can be compared to the 22-eV remoderated beam (also given in table 4) from [13]. Both quantities are found to be higher for the primary beam.

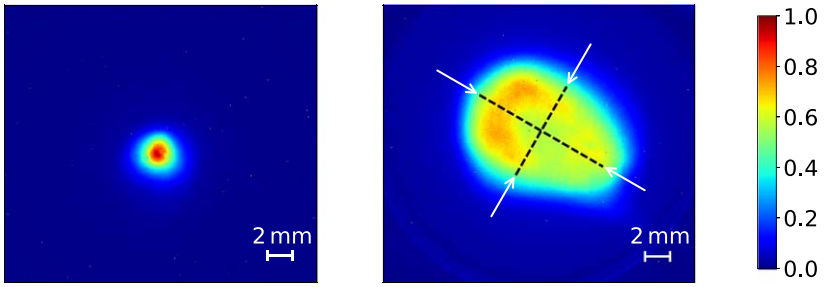

Figure 5. Normalized false color pictures of the MCP phosphor screen, showing an example spatial extent for remoderated (left) and primary (right) beams (both for 20 eV) in the six-way cross at the experiment's entrance. In the right panel the minimum and maximum FWHM is illustrated in addition. The width of each image is identical to the MCP diameter of 25 mm.

Table 4. Energy measurements of the 20-eV primary beam (p) in a uniform magnetic field of 4.8 mT for three different settings. For comparison, the results for the 22-eV remoderated beam (r) from [13] are quoted for the same magnetic field.

Type	Setting	$\bar{E}_{tot}$ [eV]	$\bar{E}_{\perp}/B_i$ [eV/mT]	$E_{\parallel}$ [eV]	$\sigma_{E_{\parallel}}$ [eV]
p	Off-center	19.85(4)	0.36(5)	18.1(3)	3.16(7)
p	Centered	19.75(3)	0.47(6)	17.5(3)	2.77(6)
p	3 mm aperture	19.8(5)	0.3(1)	18.2(8)	2.8(2)
r		22.05(7)	0.26(2)	20.8(1)	1.3(1)

4. Dipole injection and trapping experiments

4.1. Injection experiments

4.1.1. 5-eV primary beam

As shown in the previous section, the 5-eV primary beam differs mainly from its remoderated counterpart in having a larger spatial spread and a substantial admixture of electrons. We investigated whether injection of such a beam into the dipole trap is achievable and if it is affected by the electron component. Starting with the trap parameters that yielded lossless injection for the remoderated beam, the injection of the primary beam was optimized through the following parameters: the currents in the steering coils I_r and I_θ which move the beam in radial and azimuthal direction, the bias on the $E \times B$ plates $|V_{E\times B}|$, the bias on the magnet V_{mag}, the bias on the ring electrode V_{ring}, and the biases on segment 1 and segments 2-8 of the outer wall V_{seg1} and V_{seg2-8}. The resulting nominal values are given in the appendix (table A1).

Variation of the net count rate from the BGO scintillation detector aimed at the probe (signal with probe inserted minus signal with probe retracted) as I_r is varied is shown in figure 6, both with and without blocking the electron component. It is obvious that the optimization was not strongly influenced by the electron component, perhaps because the electron energy is higher than the positron energy (figure 3) and the bias voltages were optimized for positron injection. When the electrons are blocked by negatively biasing an upstream electrode, there is a slight increase in the count rate from the probe. We speculate that biasing this upstream electrode, in addition to suppressing the electron component, has some minor effect on the position (and/or shape) of the positron beam that results in slightly better injection efficiency.

For the conditions where the electrons are blocked, figure 7 shows the positron flux to the insertable probe as measured with a current-integrating amplifier while varying the probe's position. The positrons are found about half-way between the magnet and the outer wall, similar to the distribution of the 5-eV remoderated beam previously measured under similar experimental conditions. The injection efficiency—determined by the fraction of the maximum positron flux at the probe to the flux at the upstream target—is 61(7)%, which is significantly lower than for the remoderated beam (table 5), which can be injected without losses [9]. In further independent optimization scans, the injection efficiency never exceeded 66%.

4.1.2. 20-eV primary beam

Experiments with the 20-eV primary beam allow investigation of the injection of positrons with higher energy and comparison to the results for the 5-eV primary beam. Note that for the creation of a pair plasma higher injection energies could lead to higher temperatures, which would make it harder to achieve a small Debye

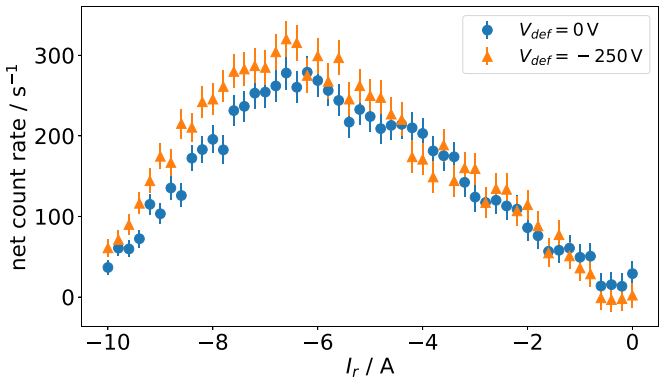

Figure 6. Variation of the net count rate of the BGO scintillation detector while changing the current in one of the steering coils at the entrance of the dipole trap. The view of the scintillation detector is collimated to an equatorial slice of the dipole trap including the movable probe but excluding the injection port side (the geometry is shown in figure 2). The difference between the count rate with the probe fully inserted and fully retracted is shown. The scan is shown for the same condition with (orange triangles) and without (blue circles) blocking the electron component of the beam through a negative bias voltage to the upstream blocking electrode.

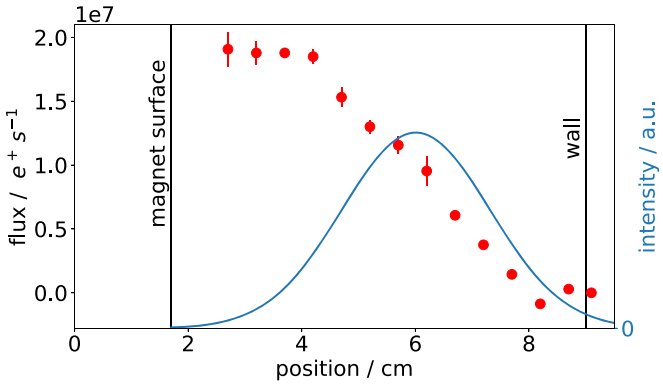

Figure 7. Variation of the 5-eV positron flux with position of the movable probe in the equatorial plane of the dipole chamber. The flux is measured with a current-integrating amplifier connected to the probe. As all particles intersecting any part of the probe are measured, this represents an integrated measurement from the probe position out to the wall. The mean positron location of (6.01 ± 0.09)cm and spread of (1.8 ± 0.2)cm are determined from a fit to a complementary error function (not shown). The blue line shows the derivative of the fit, giving an indication of the radial distribution of the positron orbits. The experimental settings for this measurement are given in the appendix (table A1).

Table 5. Injection efficiencies and resulting injected fluxes to date in the supported dipole trap for the 5-eV remoderated (r) and primary (p) beams and the 20-eV primary beam.

Energy [eV]	Type	Injection efficiency	Injected flux [10^7 e^+/s]
5	r	1 ± 0.04	1.8 ± 0.5
5	p	0.61 ± 0.07	1.4 ± 0.6
20	p	0.6 ± 0.1	8 ± 1

length. We are nonetheless interested in their injection efficiencies, since we could possibly compensate for this with a higher injection rate, subsequent cooling, or both.

The optimization was guided by the assumption that the injection process remains the same for positrons of arbitrary energy; i.e., magnetic mirroring and electrostatic reflections (from the ring electrode and/or outer wall segment 1 (figure 2)) alternate until the confinement region is reached (as described in [9]). Figure 8 shows the net annihilation rate from the probe (indicating successful injection) versus the bias on the ring electrode (left, with (orange) and without (blue) positive bias on the outer wall segment 1) and versus the bias on the outer wall segment 1 (right, with (orange) and without (blue) positive bias on the ring electrode). In fact, optimal injection requires about +20V on each of these electrodes, which is close to the beam energy. All optimized values for the control parameters are given in the appendix (table A1).

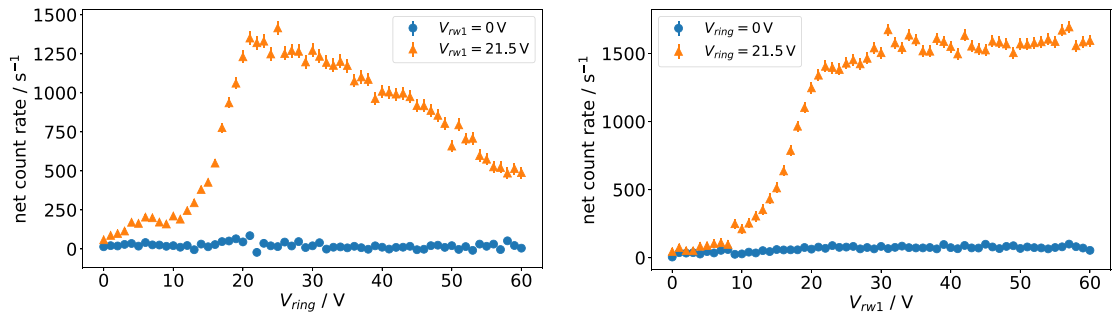

Figure 8. Variation of the net count rate of the BGO scintillation detector while changing the bias voltage on (left) the ring electrode, and (right) the outer wall segment 1 (figure 2). The view of the detector is the same as for the data in figure 6. The difference between the count rate with the probe fully inserted and fully retracted is shown. The left scan is shown for conditions with the outer wall segment 1 biased positively (orange triangles) and grounded (blue circles). The right scan is shown with the ring electrode biased positively (orange triangles) and grounded (blue circles). The remaining parameters are fixed.

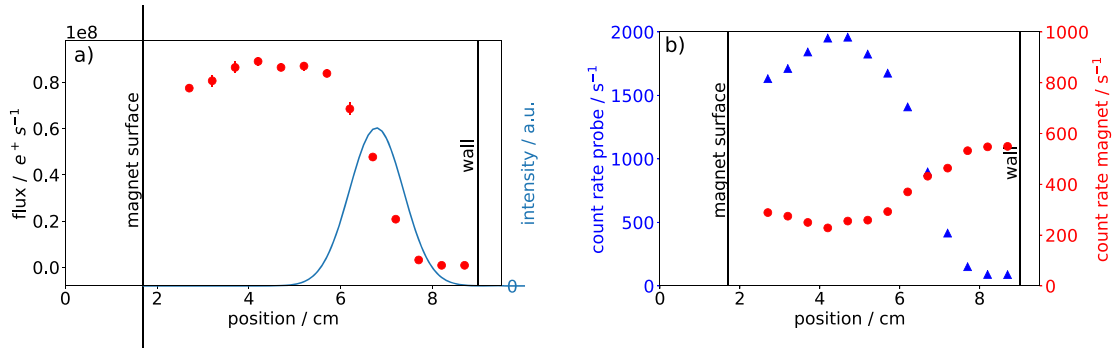

Figure 9. (a) The radial distribution of positron orbits for the 20-eV primary beam (compare to figure 7 for the 5-eV primary beam), measured with a current-integrating amplifier. The derivative of the fit to a complementary error function (blue curve) yields a mean positron location of (6.78 ± 0.04)cm and a spread of (0.82 ± 0.09)cm. (b) Variation of the count rate from the BGO scintillation detectors while varying the position of the probe. As shown in figure 2, the detectors view either the equatorial plane containing the probe (blue triangles, left y-axis) or the lower edge of the $E \times B$ plates and the upper edge of the magnet case (red circles, right y-axis). The experimental settings for these measurements are given in the appendix (table A1).

The positron flux to the radially insertable probe versus its position yields a mean positron location somewhat further away from the magnet as compared to the 5-eV beam (figure 9(a)). This might be a result of grounding the magnet for these measurements with the 20-eV beam. Unlike the case for the 5-eV beam, where the magnet was biased to −5 V, no improvement in injection efficiency was observed for non-zero bias voltages, but the spatial distribution of positron orbits might have been affected. This effect has been noticed in other experimental campaigns and is also seen in simulations that will be reported in a future publication [17].

The maximum positron flux is observed at a radius of ≈4 cm and corresponds to 60(10)% of the total incoming positron flux. Although no further increase of the injection efficiency could be achieved, this result represents $(8 \pm 1) \cdot 10^7\ e^+$ /s—a record flux of positrons injected into the supported dipole trap to date (table 5).

It should be noted that the radially integrated flux does not reach a saturated level for deep insertions but, rather, decreases (figure 9(a)), in contrast to what is seen for the 5-eV remoderated and primary beam. The corresponding annihilation signal from the probe (shown in figure 9(b)) reproduces the result from the flux measurement; it also shows an annihilation signal from a second BGO detector viewing a portion of the magnet (and some fraction of the $E \times B$ and shield plates as shown in figure 2). This data shows that as the signal from the probe decreases for small radii the signal from the other detector increases.

4.1.3. Complementary simulations

The unexpected features seen in the injection measurements with the primary beam, namely the injection efficiency saturating at values well below 100% and the non-monotonic integrated spatial profiles for 20-eV positrons, have been explored using single-particle simulations with our code AlGeoJ [18], which has produced good agreement with previous experimental findings [9]. In the simulations, the magnetic field for guiding and confinement matched closely the experimental one as did the electrode geometry (although the magnet support was omitted).

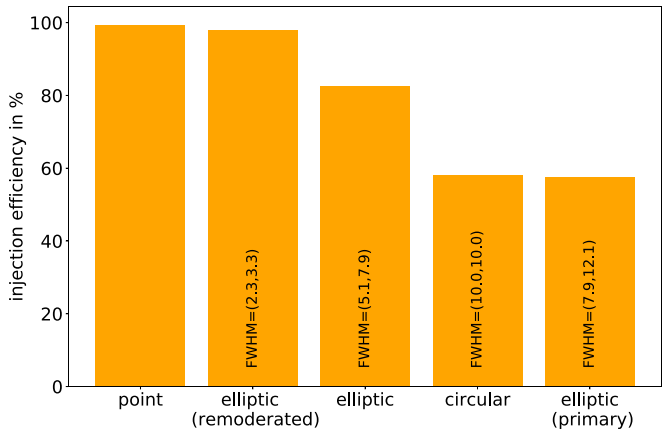

Figure 10. Comparison of the injection efficiency for simulated sources of different spatial extent but the same energy distribution. For each simulation 1000 particles were initialized for the settings described in the text. The distributed sources have a Gaussian spatial profile with the FWHM (in millimeter) as given in the figure.

First, the theoretically achievable injection efficiency—defined as the fraction of initialized particles reaching a 1-cm wide band in the equatorial plane on the probe side—was maximized as a function of the steering coil currents, electrode bias voltages and source position. The particle source is idealized as a disk ($r_d = 20$ mm) with a 2D Gaussian spatial distribution (FWHM $= 10$ mm) which is placed on the midplane of the upstream six-way cross; the mean energy distribution was matched to the measured values of the 5-eV primary beam from table 3 with $B_i = 4.8$ mT. For each run, 500 particles were initialized. The optimization yielded values for the control parameters as given in the appendix (table A1) with radial and azimuthal source offsets of $\Delta x_s = 1$ mm and $\Delta z_s = 2$ mm. The resulting injection efficiency was 59%, similar to the experimental findings.

The simulations were then run at these settings with sources of different size and shape but identical energy distribution. The injection efficiency decreases with increasing source size (figure 10). While an elliptical source with dimensions of the remoderated beam yields lossless injection, for an elliptical source with dimensions of the primary beam significantly fewer particles are injected successfully. The limited injection efficiency of the primary beam seen in the experiment may therefore be attributed to its larger spatial spread. An alternative way to state the result is that the dipole trap has a limited spatial 'injection window' which can accommodate the entire remoderated beam but only a fraction of the primary beam. The area of this window can be estimated from the spatial spread of the primary beam (table 2) and the injection efficiency (table 5). This raises the question of whether the spatial spread of the primary beam can be reduced in a near-lossless fashion in order to better fit this window and achieve higher injection efficiency. This is, in principle, possible by increasing the guiding magnetic field strength, but future work will have to determine whether this would lead to unwanted effects such as requiring the use of higher injection energy to avoid magnetic mirroring.

Second, the novel shape of the integrated spatial profiles for 20-eV positrons (shown in figure 9) is investigated by focusing on two parameters: the actual probe geometry and the energy of the particles. Note that particles in the dipole trap experience a motion with three characteristic frequencies and spatial scales. They gyrate rapidly about the magnetic field while bouncing between the high field regions near the poles of the magnet, and drift toroidally due to the magnetic field gradient and curvature. These toroidal drifts depend on the particles' parallel and perpendicular energies. The realistic geometry of the probe consisting of a 'probe holder' and a 'probe head' was added to the simulations. To begin with, the number of particles hitting the probe and the number of particles passing the probe location (but not striking the probe) were recorded for different radial insertions. The simulations were run with an elliptical particle source, once with the spatial parameters (table 2) and energy characteristics of the 20-eV primary beam (table 4, with $B_i = 4.8$ mT) and once with parameters of the 5-eV remoderated beam from [13]. The respective control parameters are given in table A1. The resulting integrated spatial profiles are shown in figures 11(a) and (c). For both energies, the simulation results agree qualitatively with the experimental findings. For 20-eV positrons, the profile signal decreases while the number of particles that are able to bypass the probe increases when the probe is positioned very near to the magnet (similar to the signal from the second BGO detector in figure 9(b)). In contrast, the profile signal for 5-eV positrons saturates at small radii as does the number of bypassing particles.

In another simulations, we measured the distance between each pair of consecutive crossings of the equatorial plane for particles drifting azimuthally from 90° to 180° (where 0° is the azimuth of injection and 180° is the location of the probe). This average 'bounce distance' versus the average orbit radius in the equatorial plane for each particle is shown for the two sources in figures 11(b) and (d). For both energies, most particles intersect the

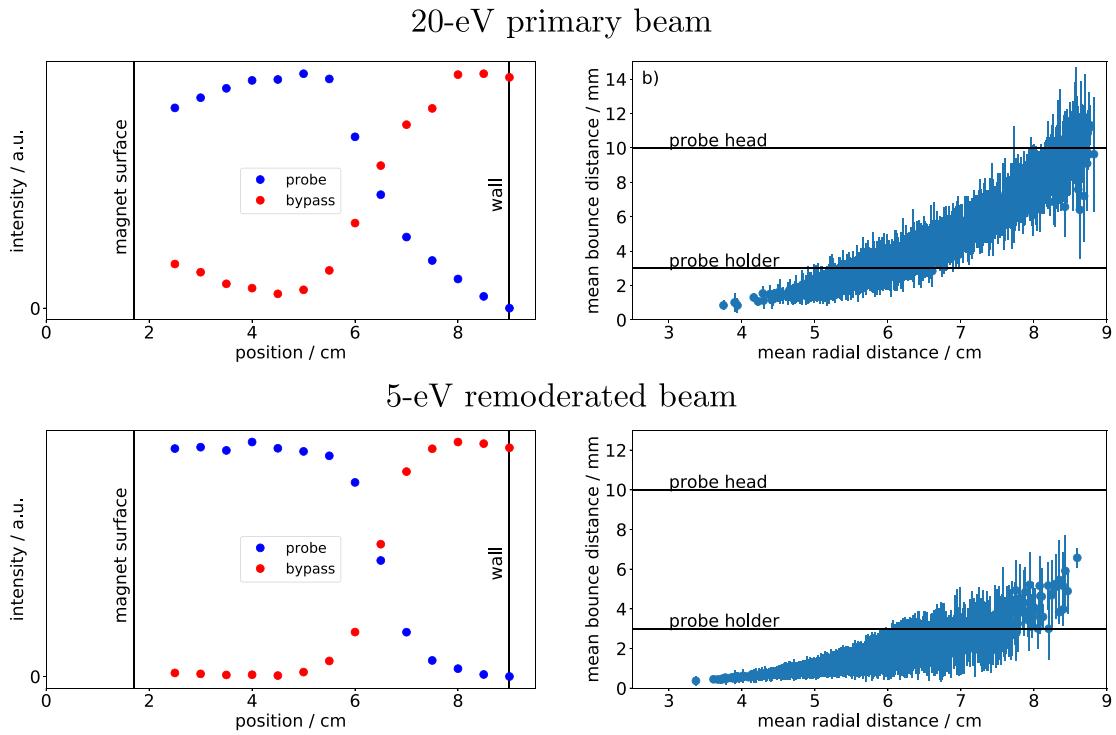

Figure 11. Simulation results for elliptical sources at the upstream injection site with (top) 20-eV primary beam parameters and (bottom) 5-eV remoderated beam parameters. Panels (a,c) show the normalized radial dependence of the number of particles hitting (blue) and bypassing (red) the probe. Panels (b,d) show the average bounce distance (distance between consecutive crossings of the equatorial plane of the dipole trap) versus average radial position in the equatorial plane for particles moving azimuthally from 90° to 180°. The horizontal lines indicate the width of the probe head and holder in the equatorial plane, respectively.

probe head when it is inserted to the radial location of their orbit. However, many 20-eV particles (top row) have equatorial bounce distances exceeding the diameter of the probe holder and are thus, at least in principle, able to miss the probe. In contrast, the bounce distance of the majority of the 5-eV particles (bottom row) is smaller than the diameter of the probe holder and thus very few miss the probe. To conclude, the shape of the integrated spatial profiles seen in the experiment results from both the particle energy and the probe geometry. In future experiments, a modified probe geometry will be used to eliminate this feature and produce monotonic integrated spatial profiles for 20-eV positrons. Such a modification has been tested successfully in experiments with electrons.

4.2. Confinement

Using the newly developed 20-eV primary beam, we investigated trapping of positrons with higher energies and in larger numbers than in previous work [8]. For these experiments, the view of one BGO scintillation detector was widened to include the entire trap, and confinement experiments were conducted using repeated inject-trap-dump cycles. One cycle proceeds as follows: during the injection phase, the blocking electrode at the experiment's entrance is grounded and all trap electrodes are set to their respective bias voltages for optimal injection. The trapping phase begins when the blocking electrode is raised to a potential substantially exceeding the beam energy; at the same time, the bias voltages on the $E \times B$ plates and outer wall segment 1are set to ground. At some delay time Δt relative to the onset of trapping, a 10-ms counting window begins. All annihilation gamma counts from the confinement region that are detected within that window are summed and assigned to this value of Δt. The delay time is then varied to obtain the number of annihilation gammas from positrons that are lost from the trap as a function of time. The trapping phase ends when the trap electrodes, which were grounded during the confinement phase, are returned to the bias voltages used for injection. In the following 10–20 microseconds, any remaining trapped positrons are assumed to be lost [8], i.e. 'dumped'. In a typical cycle, the end of the trapping phase occurs well after the end of the 10-ms counting window; however, the timing sequence can alternately be configured so that the counting window overlaps the end of the trapping phase. The signal then includes the 'dump' signal and provides an indication of whether positrons were still left in the trap at the end of the trapping phase. The next cycle begins with the grounding of the blocking electrode at the experiments entrance. These cycles are repeated 4000 times for each delay time.

We investigated the influence of the bias voltage to the ring electrode on the positron loss. It had been seen earlier that asymmetries in the electrostatic trap potential can be disadvantageous for particle confinement. To explore this

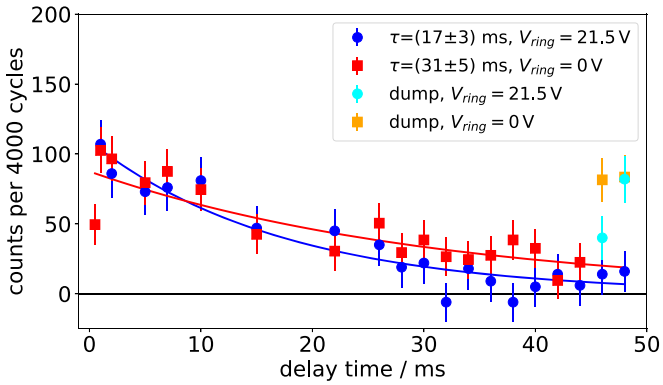

Figure 12. Annihilation signal from a detector viewing the entire confinement region measured per 4000 trapping cycles for various counting delay times. The two data sets are for a ring electrode that was biased during the entire confinement cycle (blue circles) and a ring electrode that was grounded during the trapping phase (red squares). The solid lines are the exponential fits to the data with decay times given in the legend. In addition, two data points including the 'dump' signal are shown for two delay times for a biased (cyan circles) and a grounded (orange squares) ring electrode, respectively.

aspect, we performed experiments with two conditions. The injection parameters are given in table A1 and were the same for both conditions. For one case the ring electrode bias was maintained during the trapping phase, while for the second case, it was grounded. The resulting background-subtracted data is shown in figure 12 (blue circles and red squares) together with the respective exponential fits. Removing the top-down asymmetry introduced by a non-zero bias voltage on the ring electrode during the trapping phase leads to a significant reduction in the loss rate, in this case by nearly a factor of two. In addition, two data points were taken for each condition that included the 'dump' signal (cyan circles and orange squares in figure 12). These measurements were the first indications that positron could be trapped orders of magnitude longer than the several milliseconds reported earlier [8]. Longer trapping times have been explored more completely for 5-eV positrons and published in references [19, 20]. We are optimistic that similar long trapping times can be achieved with 20-eV positrons in future optimized experiments.

5. Summary

Motivated by the search for sources with higher positron fluxes for the APEX project, we have adjusted the primary positron beam from the NEPOMUC source to energies of 5 and 20 eV. The beams were characterized in terms of flux, spatial spread and energy. Their suitability for injection into the supported dipole trap with a scheme similar to that used previously in [8, 9] has been confirmed. Although the resulting injection efficiencies of 60%–70% are lower than those observed for the remoderated beam due to the primary beam's larger spatial spread, the 20-eV primary beam nevertheless yields the maximum positron flux injected into the dipole trap to date. Once in the trap, the primary positrons can be found at similar radii as in experiments with the remoderated beam. At 20 eV, the observed integrated radial profiles are non-monotonic due to positrons being able to bypass the probe. Finally, first trapping experiments with the 20-eV primary beam revealed that a top-down asymmetry in the electrostatic trapping potential is disadvantageous for long particle confinement.

To summarize, the primary beam at low energies, after further optimization, is a promising candidate to increase the absolute numbers of positrons for the APEX project. While it can be injected directly into the dipole trap, it may also be used to fill a buffer-gas trap to provide dense positron pulses—a scheme which has been proposed (in conjunction with a high-field trap) for the final pair-plasma project [1]. A number of strategies for loading positrons (and electrons) into the field of a levitated dipole trap are being explored. If $E \times B$ drift injection is used, either source must be matched to the injection window identified in the experiments and simulations presented here. This will be particularly important for pulses starting in a high magnetic field, as will be the case when using a buffer-gas or high-field trap.

Acknowledgments

This work is based upon experiments performed at the NEPOMUC positron beam facility operated by FRM II at the Heinz Maier-Leibnitz Zentrum (MLZ), Garching, Germany. The work received funding from the European Research Council (ERC) under the European Unions Horizon 2020 research and innovation programme under grant agreement No 741322. Furthermore, the authors thank the DFG (No. Hu 978/15–1, Sa 2788/2–1), JSPS KAKENHI (No. 25707043, No. 16KK0094) and the Helmholtz Postdoc Programme (EVS) for funding.

Appendix Control parameters

The control parameters used for the experiments and simulations presented in the main text are summarized in table A1.

Table A1. Control-parameter settings for injection and trapping experiments, and simulations presented in this work.

Section	Figure	Energy [eV]	I_r [A]	I_θ [A]	$\lvert V_{E\times B}\rvert$ [V]	V_{mag} [V]	V_{ring} [V]	V_{seg1} [V]	V_{seg2-8} [V]
4.1.1	7	5	−6.6	2	180	−5	12	12	0
4.1.2	9	20	−4.5	5.5	200	0	21.5	30	0
4.1.3	10	5	−6.5	-0.5	240	10	6	11	0
	11(a), (b)	20	−4.5	5.5	200	0	21.5	30	0
	11(c), (d)	5	−6.6	2	180	−5	12	12	0
4.2	12	20	−4.5	5.5	200	0	21.5	30	0

ORCID iDs

J Horn-Stanja https://orcid.org/0000-0001-8305-4300
U Hergenhahn https://orcid.org/0000-0003-3396-4511
T Sunn Pedersen https://orcid.org/0000-0002-9720-1276

References

[1] Sunn Pedersen T, Danielson J R, Hugenschmidt C, Marx G, Sarasola X, Schauer F, Schweikhard L, Surko C M and Winkler E 2012 Plans for the creation and studies of electron-positron plasmas in a stellarator *New J. Phys.* **14** 035010
[2] Alfvén H 1950 *Cosmical Electrodynamics* (Oxford University Press)
[3] Van Allen J A 1997 *Discovery of the Magnetosphere (History of Geophysics)* vol. 7 (American Geophysical Union)
[4] Yoshida Z, Saitoh H, Morikawa J, Yano Y, Watanabe S and Ogawa Y 2010 Magnetospheric vortex formation: self-organized confinement of charged particles *Phys. Rev. Lett.* **104** 235004
[5] Boxer A C, Bergmann R, Ellsworth J L, Garnier D T, Kesner J, Mauel M E and Woskov P 2010 Turbulent inward pinch of plasma confined by a levitated dipole magnet *Nat. Phys.* **6** 207
[6] Hugenschmidt C, Piochacz C, Reiner M and Schreckenbach K 2012 The NEPOMUC Upgrade and advanced positron beam experiments *New J. Phys.* **14** 055027
[7] Hugenschmidt C, Ceeh H, Gigl T, Lippert F, Piochacz C, Reiner M, Schreckenbach K, Vohburger S, Weber J and Zimnik S 2014 Positron beam characteristics at NEPOMUC Upgrade *J. Phys.: Conf. Ser.* **505** 012029
[8] Saitoh H, Stanja J, Stenson E V, Hergenhahn U, Niemann H, Sunn Pedersen T, Stoneking M R, Piochacz C and Hugenschmidt C 2015 Efficient injection of an intense positron beam into a dipole magnetic field *New J. Phys.* **17** 103038
[9] Stenson E V *et al* 2018 Lossless positron injection into a magnetic dipole trap *Phys. Rev. Lett.* **121** 235005
[10] Stoneking M R *et al* 2018 Toward a compact levitated superconducting dipole for positron-electron plasma confinement *AIP Conf. Proc.* **1928** 020015
[11] Gabrielse G *et al* 2002 Stacking of cold antiprotons *Phys. Lett.* B **548** 140–5
[12] Rosenbusch M, Atanasov D, Blaum K, Borgmann Ch, Kreim S, Lunney D, Manea V, Schweikhard L, Wienholtz F and Wolf R N 2014 Ion bunch stacking in a Penning trap after purification in an electrostatic mirror trap *Appl. Phys.* B **114** 147
[13] Stanja J, Hergenhahn U, Niemann H, Paschkowski N, Sunn Pedersen T, Saitoh H, Stenson E V, Stoneking M R, Hugenschmidt C and Piochacz C 2016 Characterization of the NEPOMUC primary and remoderated positron beams at different energies *Nucl. Instr. and Meth. in Phys. Res.* A **827** 52–62
[14] Pastuszka S, Hoppe M, Kratzmann D, Schwalm D, Wolf A, Jaroshevich A S, Kosolobov S N, Orlov D A and Terekhov A S 2000 Preparation and performance of transmission-mode GaAs photocathodes as sources for cold dc electron beams *J. Appl. Phys.* **88** 6788
[15] Hugenschmidt C, Brunner T, Mayer J, Piochacz C, Schreckenbach K and Stadlbauer M 2008 Determination of positron beam parameters by various diagnostic techniques *Appl. Surf. Sci.* **255** 50
[16] Gonzalez L A, Angelucci M, Larciprete R and Cimino R 2017 The secondary electron yield of noble metal surfaces *AIP Adv.* **7** 115203
[17] Nissl S *et al* 2020 in preparation
[18] Nissl S 2018 Numerical investigations into injection and confinement of single particles in a magnetic dipole trap *Master's Thesis* Technische Universität München
[19] Hergenhahn U *et al* 2018 Progress of the APEX experiment for creation of an electron-positron pair plasma *AIP Conf. Proc.* **1928** 020004
[20] Horn-Stanja J *et al* 2018 Confinement of positrons exceeding 1 s in a supported magnetic dipole trap *Phys. Rev. Lett.* **121** 235003